Revealing Additional Size-Dependent Defect Suppression Channels Governing Detectivity in InAs Colloidal Quantum Dot Photodiodes

Stefan Zeiske, Hyeong Woo Ban, Xubiao Li, Bin Deng, Rafael López-Arteaga, Ubaid H. Kazianga, Moon Gyu Han, Tae-Gon Kim, Bin Chen, and Edward H. Sargent

DOI 10.1021/acs.nanolett.5c04477

Title: Revealing Additional Size-Dependent Defect Suppression Channels Governing Detectivity in InAs Colloidal Quantum Dot Photodiodes

Authors and Affiliations: Stefan Zeiske[1], Hyeong Woo Ban[1], Xubiao Li[1], Bin Deng[1], Rafael López-Arteaga[1], Ubaid H. Kazianga[1], Moon Gyu Han[2], Tae-Gon Kim[2], Bin Chen[1,*], and Edward H. Sargent[1,3,4,*]

[1]Department of Chemistry, Northwestern University, Evanston, IL, 60208, USA

[2]Samsung Advanced Institute of Technology, Samsung Electronics, Suwon 16678, Republic of Korea

[3]Department of Electrical and Computer Engineering, University of Toronto, Toronto, Ontario M5S 3G4, Canada

[4]Department of Electrical and Computer Engineering, Northwestern University, Evanston, IL, 60208, USA

*corresponding author: bin.chen@northwestern.edu, ted.sargent@northwestern.edu

Abstract:

Indium arsenide (InAs) colloidal quantum dot (CQD) photodiodes combine tunable bandgaps with solution processing, offering a versatile platform for infrared detection. Using highdynamic-range external quantum efficiency (HDR-EQE) measurements, we probe defect signatures and quantify their impact on performance. Analysis of Urbach tails and Gaussian sub-bandgap states shows that trap densities decrease with increasing nanocrystal size, exceeding predictions from simple surface-to-volume scaling and underscoring the influence of surface chemistry on bandedge disorder. These defect states affect the dark saturation current ($J_!$), enabling us to estimate their contribution to detectivity and noise. The results connect nanocrystal size, defect population, and device performance, distinguishing intrinsic trapmediated effects from extrinsic loss channels. We find that while intrinsic defects play a role, today's InAs CQD photodiodes are primarily limited by contact and interface properties, highlighting these as key targets for further improvement.

Keywords:

Colloidal quantum dots, InAs, photodiodes, trap states, high-dynamic range external quantum efficiency, sub-bandgap absorption, photocurrent spectroscopy

Main:

Colloidal quantum dots (CQDs) are semiconductor nanocrystals that have emerged as versatile active materials for photodetectors, photovoltaics, and other optoelectronic devices, owing to their size-tunable bandgaps, solution processing, and compatibility with low-cost fabrication.[1–3] Colloidal quantum dot research focuses largely on II–VI materials such as CdSe, PbS and HgTe, known for their superior optoelectronic properties, but containing regulated heavy metals; and III–V materials such as InAs and derivatives, which are heavy-metal free and promising for near-infrared detection.[4–8] However, the overall performance of CQD-based photodiodes remains constrained by non-idealities associated with defect states, which act as recombination centers, trap charges, and induce electronic noise.[1,9–13]

Defects in CQDs originate from diverse sources and influence their optoelectronic properties. Surface oxidation and etching processes, driven by exposure to oxygen and moisture, result in the formation of oxide and hydroxide species that introduce defect states detrimental to device performance.[14–16] Unsaturated surface atoms further contribute by disrupting the periodic potential of the nanocrystal lattice, leading to localized trap states.[17,18] Impurities incorporated during synthesis or as a result of doping modify the defect landscape through the creation of shallow trap states, lattice distortions, and doping compensation effects.[19–21] Heterostructured CQDs, such as core/shell architectures, exhibit interfaces marked by lattice strain, stoichiometric imbalance, and heterocovalent bonding, which exacerbate trap densities and alter carrier dynamics, ultimately influencing detector device stability and efficiency.[22–25]. These defect-mediated processes militate against charge transport and enhance recombination, limiting critical performance parameters.

A key photodetector performance metric is the specific detectivity, defined as $D^* = q\lambda\&A\Delta f/hc \times \mathrm{EQE}/\overline{i_{\mathrm{noise}}}$, with i_{noise} the noise current, q the elementary charge, h Planck's constant, Δf the electrical bandwidth, c the speed of light, λ the wavelength, A the detector area, and EQE the external quantum efficiency.[26] In CQD devices, extending the operational window deep into the infrared demands larger nanocrystals, a synthetic challenge that grows rapidly with longer wavelength. Optical and electrical gain strategies can increase EQEs to beyond $10^{(}$%, yet such enhancements do not overcome the fundamental detectivity ceiling set by dark-current–induced noise, an effect that dominates especially in devices having bandgaps to detect long wavelengths. [27]

The dark current in CQD photodetectors (PDs) under reverse bias comprises two distinct components: the dark saturation current density ($J_!$) and the shunt current density (J_{shunt}). The latter originates from fabrication-induced imperfections that create unintended leakage pathways, whereas $J_!$ is dictated by thermally activated radiative and non-radiative processes within the CQD active layer–such as direct band-to-band transport or trap-mediated transitions–or at contacts, such as minority carrier injection from the electrodes. Following $J_! \propto \exp(-E_{\mathrm{a}}/kT)$, the activation energy (E_{a}) reflects the dominant dark current mechanism, k the Boltzmann constant and T the temperature.[10,12] $J_!$ describes a lower bound on the noise current and thus also bounds the achievable specific detectivity of CQD PDs. Although trap states–often linked to CQD surface defects–have been reported across a broad range of CQD materials, their impact on the dark current mechanisms in CQD PDs warrants further study.

In this work, we study size-tuned colloidal InAs quantum dot photodiodes using high–dynamicrange EQE spectroscopy, seeking to identify sub-bandgap defect states and assess their impact on critical device performance metrics such as dark current and detectivity. Sub-bandgap EQE features are described using a model that includes an Urbach tail, capturing band-edge absorption; and a Gaussian distribution of localized states. Studies as a function of nanocrystal size reveals a reduction in total defect density dominated by the suppression of surface traps. We find that while smaller InAs quantum dots follow the expected surface-to-volume scaling of defect density, larger nanocrystals exhibit a pronounced reduction in defect density, indicating the presence of additional defect suppression pathways. Analysis of dark current in these InAs photodiodes shows that defect states impose a limit on the dark saturation current density, constraining not only the photodetector noise and best-case specific detectivity of InAs CQD photodiodes, but also setting fundamental performance bounds for related InAs-based devices. At the same time, our results indicate that the performance of today's best InAs CQD photodiodes is limited less by intrinsic nanocrystal quality and more by extrinsic factors such as contacts and interfacial layers. These findings establish HDR-EQE as a powerful tool for defect characterization, while also pointing the field toward the critical challenge of improving device architectures to fully unlock the potential of InAs nanocrystal photodetectors.

Results

We fabricated a series of InAs CQD PDs incorporating nanocrystals (NCs) with tuned sizes (see **Supplementary Materials** for synthesis and device fabrication procedures). EQE spectra of these PDs are presented (**Fig. 1a**, **Figs. S1** and **S2**) normalized to the first excitonic absorption peak and their maxima—from ∼940 nm to ∼1320 nm—are consistent with the size-dependent optical absorption features observed in the absorbance spectra. All EQE measurements were performed under zero-bias (short-circuit) conditions.

To probe sub-bandgap states, we performed high–dynamic-range (HDR) EQE measurements extending well below the bandgap energy (blue solid lines, **Fig. 1b**), revealing a pervasive lowenergy feature. The CQD active layer thickness was intentionally kept at ∼100 nm to minimize low-finesse cavity interference, which is known to distort sub-bandgap EQE features in thinfilm photodiodes[28–30]. Our goal here was to keep the link between estimated sub-gap signatures and electrooptically-active sub-bandgap states.

For the analysis, the fitting was restricted to the sub-bandgap region, i.e. to photon energies well below the first excitonic peak position, ensuring that the extracted parameters reflect defect-related absorption rather than quantum confinement features. We can fit an analytical model (white dashed lines) to these data that comprises two additive terms: an Urbach tail describing exponential band-edge absorption (green solid lines) and a Gaussian distribution (purple solid lines): $\mathrm{EQE}(E_{\mathrm{ph}}) = A\ \exp\mathrm{BC}E_{\mathrm{ph}} - E_{\mathrm{g}}\mathrm{D}/E_{\mathrm{U}}\mathrm{E} + B\ \exp\ \mathrm{H}-\ \mathrm{C}E_{\mathrm{ph}} - E_{\mathrm{t}}\mathrm{D}^{0}/2\sigma^{0}\mathrm{J}$, where

E_{ph} is the photon energy, E_{g} the bandgap, E_{t} the characteristic energy of a sub-bandgap (low energy) state below the band edge, E_{U} the Urbach energy, and σ is the Gaussian width; A and B are weighting factors. Details of the fitting procedure, parameter uncertainties, and error propagation for the estimated defect densities are provided in Supplementary Note S1.

The extracted Urbach energies E_U are $\sim 19-26$ meV, consistent with reported values for other colloidal quantum dot systems such as PbS (see **Fig. 1c**).[31] Defined as the slope of the exponential absorption tail at the band edge, E_U is typically interpreted as a proxy for energetic disorder, which increases with carrier–phonon interactions and directly impacts charge transport. In colloidal quantum dots, Jean et al. demonstrated that E_U is highly sensitive to surface chemistry and processing conditions: complete ligand passivation and dense quantum dot packing sharpen the band edge, whereas weaker passivation or degradation broaden the tail.[31] They further reported a pronounced size dependence, with smaller dots exhibiting larger E_U, and proposed that size-independent trap states entering the bandgap could underlie this trend. However, a distinct sub-bandgap feature was observed only in a single larger nanocrystal sample, which they attributed to a trap state; its absence in other sizes prevented conclusive validation of their claim. Erslev and co-workers further showed that intentionally broadened size distributions do not significantly affect E_U, indicating that polydispersity primarily manifests as excitonic peak broadening.[32]

Our measurements similarly reveal a clear size dependence of E_U: the smallest nanocrystal ($E_g \approx 1.25$ eV) exhibits $E_U \approx 25$ meV, while the largest ($E_g \approx 0.88$ eV) shows $E_U \approx 18$ meV. In addition, we observe a universally present sub-bandgap state across differently sized InAs nanocrystals (Fig. 1b). The characteristic energy of this state, E_t, extracted from the Gaussian component of our fits, resides $\sim 0.1-0.2$ eV below the respective band edges (black line, **Fig. 1d**), yet well above the mid-gap (gray dashed line), and shifts with nanocrystal size. We therefore associate this low energy state with defects, while the persistence of a distinct Urbach tail reinforces its assignment as an intrinsic band-edge property rather than a direct manifestation of discrete traps. Complementary current deep-level transient spectroscopy (DLTS) measurements (**Fig. S3**) further support this defect-related assigned of the sub-bandgap feature captured as a Gaussian component. The slightly larger trap depths observed in DLTS compared to HDR-EQE can be attributed to the different probing mechanisms: DLTS senses thermally activated emission from deeper, electrically active traps across the depletion region; whereas HDR-EQE primarily probes optical transitions from shallower, optically active states near the band edges.

Sub-bandgap states have been reported in several studies on PbS nanocrystals. DLTS on ethanedithiol-treated solids revealed a trap ~ 0.40 eV from mid-gap, consistent with states affecting charge transport.[33] Radiative sub-bandgap features were also observed in operating devices via photoluminescence and electroluminescence, [34,35] while impedance spectroscopy identified a state ~ 0.34 eV below the conduction band. Mid-infrared photoinduced absorption revealed two trap-related bands whose energies scale with nanocrystal size, with smaller dots exhibiting lower-energy states, while ligand chemistry mainly influenced signal amplitude.[36] The energies reported in PbS closely match those we extract in InAs CQDs, where the Gaussian component lies $\sim 0.1-0.2$ eV below the band edge. The origin of such states has been variously attributed to undercoordinated surface atoms, dangling bonds, metal–chalcogen vacancies, or hybridized ligand–surface complexes. While our measurements cannot unambiguously distinguish among these scenarios, the universal presence and size-dependent energy of the sub-bandgap feature in our InAs CQDs strongly indicate that it arises from intrinsic defect states rather than extrinsic artifacts. TEM imaging (Fig. S5) and PL

characterization (Fig. S6) of the InAs CQDs confirm a narrow, Gaussian-like size distribution, supporting that the observed sub-bandgap features reflect intrinsic properties of the nanocrystals rather than effects from polydispersity or sample inhomogeneity. While our measurements do not distinguish unambiguously among these scenarios, the consistent presence and size-dependent energy of the sub-bandgap feature in our InAs CQDs, along with top-metal comparison data included in the Supporting Information (Figure S7), suggest that these states arise predominantly from intrinsic defect states rather than extrinsic artifacts.

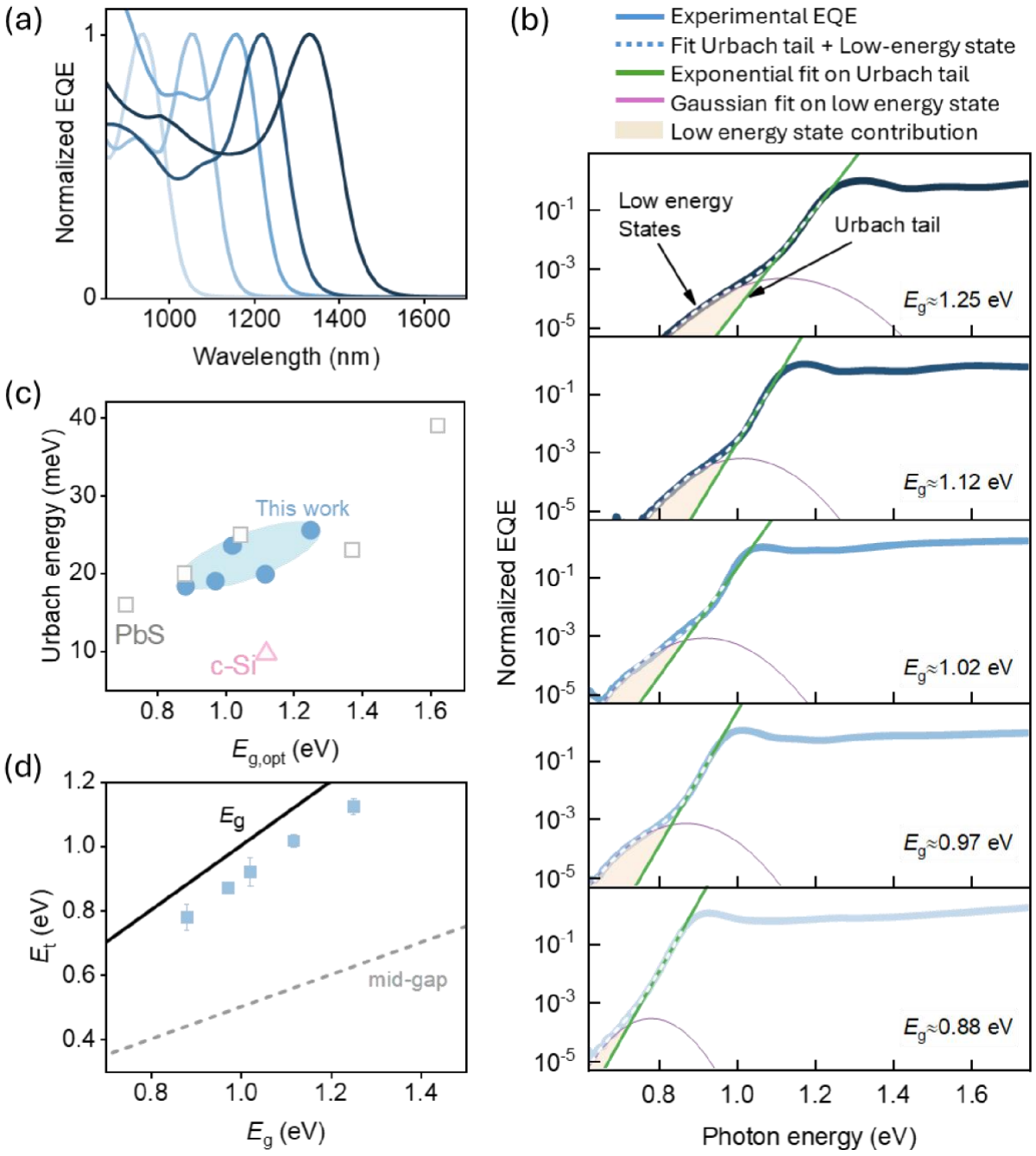

Figure 1. Sub-bandgap EQE to study states in colloidal InAs photodiodes a) Normalized external quantum efficiency (EQE) spectra aligned to the first excitonic peak for devices of various bandgaps. **b)** Sub-bandgap EQE spectra versus photon energy, with experimental data (blue lines), analytical fits (white dashed lines), and contributions from the Urbach tail (green) and low-energy defect states (purple). **c)** Urbach energies (blue symbols)

as a function of bandgap energy, with open symbols showing literature values for colloidal PbS quantum dots and crystalline silicon. **d)** Trap energy levels (symbols) extracted from sub-bandgap fits, plotted against device bandgap. Black and gray lines indicate the full bandgap and midgap energies, respectively.

Figure 2a shows the normalized defect densities, N_1, (blue symbols), obtained from Gaussian defect-tail fitting, as a function of nanocrystal diameter. Prior to normalization, the extracted defect densities were first referenced to the thickness of the corresponding CQD layers, thereby accounting for variations in nanocrystal number, volume, and absorption cross-section. A pronounced decrease in $N_{\mathrm{t,abs}}$ with increasing nanocrystal size is observed, consistent with earlier findings reported for colloidal PbS photodiodes, where larger nanocrystals similarly exhibited lower trap densities.[11] A surface-defect-dominated picture would predict a $1/d$ dependence arising from the decreasing surface-to-volume ratio (green solid line in Fig. 2a); thus, the markedly steeper trend observed here indicates that a suppression pathway is operative (red shaded area in Fig. 2a).

While surface curvature can indeed influence ligand binding, its effect on passivation efficiency is not always straightforward. In some systems, increased curvature in smaller nanocrystals facilitates tighter ligand packing and stronger binding, which can enhance surface passivation and photoluminescence. Conversely, in other cases, larger nanocrystals may still benefit from reduced curvature, as flatter surfaces can allow more ordered ligand attachment and lower densities of unsaturated surface atoms.[4] Despite that, size-dependent surface reconstructions can also reorganize surface atoms into lower-energy configurations, reducing strain and further suppressing the formation of trap states.[37] Therefore, the observed reduction in defect density with increasing nanocrystal size likely arises from a combination of geometric effects, curvature-dependent ligand interactions, and surface atomic rearrangements, rather than from surface-to-volume considerations alone.

Building on the defect analysis in our InAs CQD photodiodes through EQE analysis, we next quantify how these defect states influence the dark saturation current. Using HDR-EQE spectra from size-tuned InAs CQD PDs, we next calculated the radiative limit of the dark saturation current density, $J_!^{\mathrm{rad}} = q\int_E^{\infty} \mathrm{EQE}\varphi_{\mathrm{BB}}\, dE$, where q is the elementary charge, E the energy, and φ_{BB} denotes the black-body photon flux. Here, multiplying the black-body flux by the measured EQE provides an experimental estimate of the fraction of photons contributing to current extraction, thereby capturing the combined effects of radiative and non-radiative recombination, incomplete carrier extraction, and parasitic optical losses. This expression follows from detailed balance, which equates radiative recombination and black-body emission in the ideal diode limit.[38–40] **Figure 2b** presents the radiative dark saturation current density, $J_!^{\mathrm{rad}}$, for the InAs nanocrystal bandgap series (blue square symbols) plotted as a function of bandgap energy E_{g}. As expected from $J_! \propto \exp(-E_9/kT)$, the slope provides an estimate of the activation energy for dark current of $E_{\mathrm{a}} \approx E_{\mathrm{g}}/n_{\mathrm{id}}$, corresponding to an ideality factor of $n_{\mathrm{id}} \approx 1.7$ (black line). This value indicates that the dark current is shaped by a combination of direct band-to-band recombination ($n_{\mathrm{id}} = 1$) and defect-assisted pathways. These findings demonstrate that defect states, though not the sole driver, provide a quantitatively significant component of charge recombination in InAs CQD PDs.

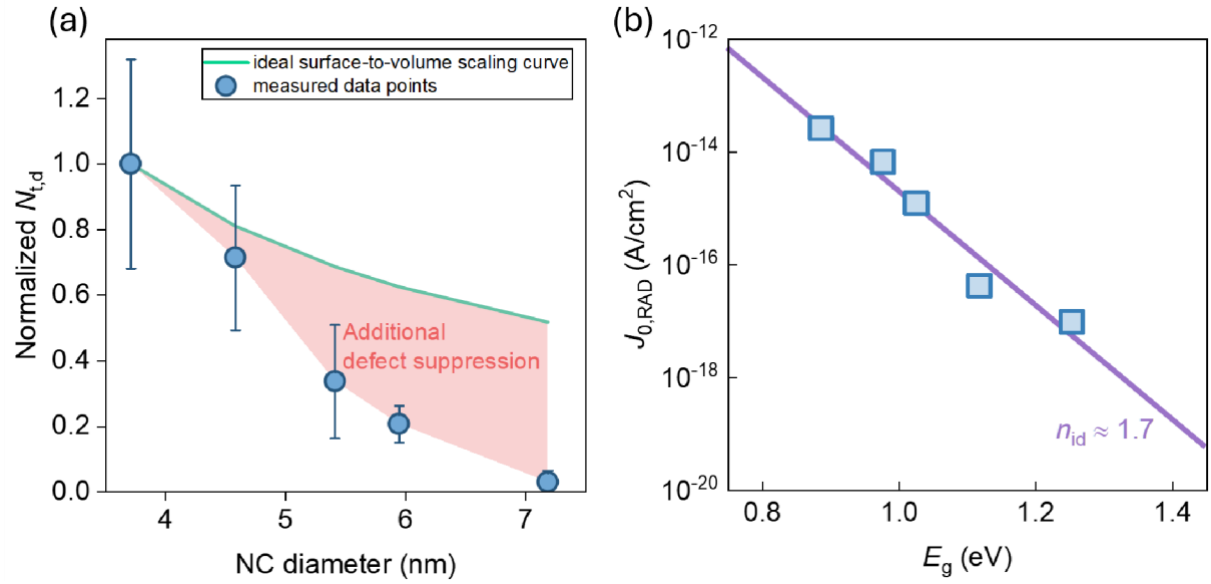

Figure 2. Impact of defects on specific detectivity a) Trap densities, calculated from Gaussian defect-tail fitting as a function of NC diameter, with $N_t \approx \sigma B$ where σ and B are fitting parameters extracted from sub-gap HDREQE spectra. Error bars represent the propagated uncertainties from the fitting parameters (see Supplementary Note S1 for details). The green solid line represents the expected $1/d$ scaling for purely surface defect-dominated scenario, while the red shaded area highlights the influence of additional defect suppression mechanisms beyond simple geometry considerations. **b)** Calculated, radiative dark saturation current density ($J^{,rad}$) of InAs PDs plotted against the bandgap energy (E_g) (blue symbols). The purple solid line is a guide to the eye which slope corresponds to an ideality factor of $n_{id} = 1.7$.

To distinguish radiative from nonradiative loss channels associated with defect states, we extrapolated the experimentally obtained sub-bandgap HDR-EQE spectra using two models: (i) an Urbach tail to represent band-to-band transitions and (ii) a Gaussian tail to describe defect-mediated absorption. **Figure 3a** illustrates this analysis for the 1.25 eV InAs CQD photodiode, where the measured HDR-EQE spectrum (blue symbols) is fitted and extended with both the Urbach (black dashed line) and Gaussian (red solid line) models. The two approaches yield markedly different $J_{0,rad}$ values at low photon energies – approximately $J_{0Urbach,rad} \approx 8 \times 10^{<=>}$ A/cm2 from Urbach model versus $J_{0Defect,rad} \approx 3 \times 10^{<=A}$ A/cm2 from Gaussian defect model – differing by more than an order of magnitude, thereby underscoring the pronounced influence of defect-mediated processes on the determination of the radiative limit (**Fig. 3b**).

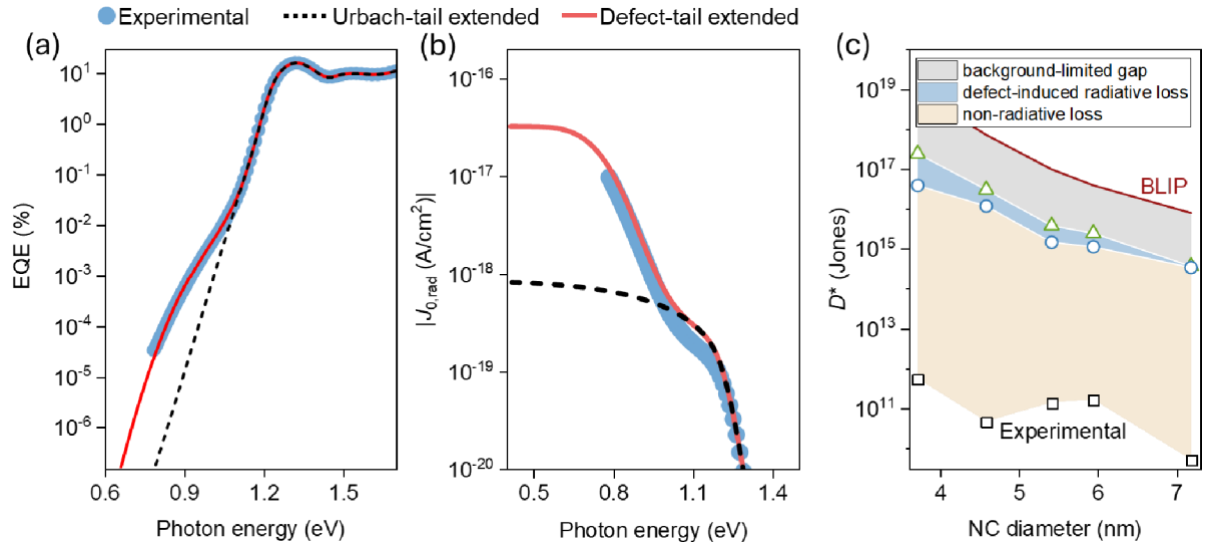

Figure 3. Detailed balance analysis and detectivity limits in CQD photodiodes a) Experimentally obtained (blue symbols) external quantum efficiency (EQE) plotted as a function of photon energy, and compared with calculated Gaussian defect-tail (black dashed line) and Urbach-tail (red solid line) extended sub-gap EQE spectrum. **b)** Calculated radiative dark saturation current density $J_{\text{"rad}}(E) = q\int_E^{\infty} \text{EQE} \times \varphi_{\text{BB}} dE$, where E the photon energy, q the elementary charge, and φ_{BB} the black body photon flux. **c)** Specific detectivity from measured dark current densities at -0.1 V applied bias voltage (black symbols), with loss contributions inferred from EQE extrapolations. Defect-induced radiative losses were calculated as $D_{\text{Urbach}^*} - D_{\text{Defect}^*}$. The red line indicates the 300 K background-limited infrared photodetector (BLIP) limit.

Using these $J_{0,\text{rad}}$ values obtained at low photon energy, we estimate the best-case specific detectivity, $D^* = q\lambda\&\overline{A\Delta f}/hc \times \text{EQE}/J_{!}$. **Figure 3c** compares forecast detectivities derived from the band-to-band (D_{Urbach^*}, based on $J_0{}^{\text{Urbach}}{}_{,\text{rad}}$), and defect-mediated ($D_{\text{Defect}^*}$, based on $J_0{}^{\text{Defect}}{}_{,\text{rad}}$) models with the background-limited infrared photodetector (BLIP) benchmark; and with experimental detectivities derived from the measured dark current of our InAs CQD PDs at -0.1 V (Fig. S4). In the defect-mediated case, nonradiative recombination through traps sets the dominant loss channel. In practice, however, additional extrinsic factors—including shunt leakage from fabrication imperfections, interface recombination at transport layers, incomplete carrier extraction, and trap-assisted tunneling—can further elevate the dark current and suppress D^*. Consequently, although the relative impact of defect-induced radiative losses decreases with smaller bandgaps (larger nanocrystals), these defects nonetheless impose a fundamental ceiling on detectivity that remains below the ideal band-to-band limit.

Urbach tailing and sub-bandgap absorption set limits on device performance, with defectmediated dark current contributing significantly to reduced detectivity in InAs CQD photodiodes. It should be noted that HDR-EQE primarily probes sub-bandgap states within ~0.2 eV of the band edge, and there is a technical limitation in sensitivity for detecting additional, deeper trap states that may also contribute to dark current. However, detectivities derived from experimental dark-current measurements suggest that the dominant bottlenecks extend beyond these intrinsic effects. Non-ohmic or non-selective contacts, localized shunting paths from film inhomogeneities, and poorly optimized interfaces can all exacerbate carrier recombination and leakage. Therefore, in addition to minimizing polydispersity and optimizing ligand surface chemistry—which primarily sharpens the band edge—and mitigating

defectrelated sub-bandgap states, interface and contact engineering remains a crucial and promising route to further enhance photodetector performance and increase detectivity, while deeper traps may also contribute additional, unresolved losses.

Discussion:

High-dynamic-range EQE measurements reveal the universal presence of defect states and their direct impact on dark saturation current, specific detectivity, and noise in InAs CQD photodiodes. Across a broad range of CQD PDs, the dark saturation current density, J_0, exhibits a universal scaling consistent with defect-mediated recombination mechanisms, imposing a fundamental upper limit on device performance. In these photodiodes, J_0 directly constraints the achievable specific detectivity, $D^* = q\lambda\left(hc\sqrt{2q|J_0|}\right)^{-1}$, and sets the noise-equivalent power, NEP $= i_{\text{noise}}/R$, where R is the responsivity and the total noise current $i_{\text{noise}} =$

$\sqrt{i_{\text{shot}}^2 + i_{\text{thermal}}^2 + i_{\text{flicker}}^2 + \cdots}$.[26] Here, the individual contributions include shot noise, ($i_{\text{shot}} = \sqrt{2qAJ_0}$); thermal noise, $i_{\text{thermal}} = \sqrt{4kT/R_{\text{sh}}}$, with R_{sh} denoting the shunt resistance); and flicker noise (i_{flicker}). Taken together, these findings highlight that the universality of defectlimited dark current reflects intrinsic material limitations and emphasize the need for precise, quantitative characterization and control of trap states—an objective directly addressed by HDR-EQE measurements.

Extending this quantitative perspective, HDR-EQE provides a direct means to evaluate subbandgap states and their contributions to key performance metrics, including dark current and radiative limits. Analysis of Urbach energies further quantifies intrinsic band-edge disorder, providing a complementary metric for material quality. While these measurements capture the steady-state impact of defects, a complete understanding of InAs CQD defect landscapes will require complementary analysis of defect energetics, densities, and recombination dynamics. Integrating optical, electrical, structural, and surface-sensitive characterization with numerical modeling will be essential to clarify the origin of defect states—whether arising from surface undercoordination, ligand–surface interactions, or atomic vacancies—and to guide actionable strategies. Collectively, these approaches point toward three primary levers for enhancing detectivity: reducing polydispersity (sharpening the Urbach tail), mitigating defect-related subbandgap absorption, and optimizing interface engineering, which appears most critical for minimizing dark current and maximizing device performance. This multifaceted approach lays the groundwork for targeted defect engineering, ultimately guiding the optimization of InAs CQD photodiodes toward their fundamental performance limits.

In summary, by investigating size-tuned InAs CQD photodiodes, we elucidate the nature and impact of sub-bandgap defect states. High–dynamic-range EQE spectroscopy revealed pervasive defect-mediated absorption features across all nanocrystal sizes, which were quantitatively modeled using a combination of Urbach tails and Gaussian defect distributions. This dual analysis enabled extraction of Urbach energies, trap densities, and defect energies, showing a pronounced decrease with increasing nanocrystal size – exceeding predictions based solely on surface-to-volume scaling and indicating the presence of additional defectsuppression mechanisms. By combining HDR-EQE with detailed balance calculations, we determined the

radiative limit of the dark saturation current and estimated the corresponding upper bounds on specific detectivity. Overall, our findings provide a rigorous framework for targeted defect engineering, guiding the optimization of InAs CQD photodiodes toward their fundamental performance limits and establishing a quantitative link between nanocrystal size, defect populations, and device performance.

Supporting Information:

Information on colloidal quantum dot synthesis and device fabrication, additional information on HDR-EQE and DLTS measurements.

Acknowledgements:

This work made use of the MatCI Facility supported by the MRSEC program of the National Science Foundation (DMR-2308691) at the Materials Research Center of Northwestern University. This work was supported by the Samsung Advanced Institute of Technology (SAIT), Samsung Electronics Co, Ltd.

Author contributions:

B.C. and E.H.S. provided the overall leadership of the project. S.Z. conceptualized the idea, designed the experiments, and measured the HDR-EQE and dark IV. U.H.K. measured the DLTS. S.Z. analyzed the data. H.B, X.L, and B.D. synthesized the colloidal InAs nanocrystals and fabricated the thin-film photodiode devices. R.L.A. contributed to data interpretation. All authors contributed to the development of the manuscript first drafted by S.Z..

Notes:

The authors declare no competing financial interests.

References:

(1) Houtepen, A. J.; Sargent, E. H.; Infante, I.; Owen, J. S.; Green, P. B.; Schaller, R. D.; Bals, S.; Zeiske, S.; Stöferle, T.; Hens, Z. Colloidal Quantum Dots for Optoelectronics. *Nature Reviews Methods Primers* **2025**, *5* (1), 1–29. https://doi.org/10.1038/s43586-025-00413-y.

(2) Liu, M.; Yazdani, N.; Yarema, M.; Jansen, M.; Wood, V.; Sargent, E. H. Colloidal Quantum Dot Electronics. *Nat Electron* **2021**, *4* (8), 548–558. https://doi.org/10.1038/s41928-02100632-7.

(3) García de Arquer, F. P.; Talapin, D. V.; Klimov, V. I.; Arakawa, Y.; Bayer, M.; Sargent, E. H. Semiconductor Quantum Dots: Technological Progress and Future Challenges. *Science (1979)* **2021**, *373* (640), 1–14. https://doi.org/10.1126/science.aaz8541.

(4) Ban, H. W.; Vafaie, M.; Levina, L.; Xia, P.; Imran, M.; Liu, Y.; Najarian, A. M.; Sargent, E.

H. Resurfacing of InAs Colloidal Quantum Dots Equalizes Photodetector Performance across Synthetic Routes. *J Am Chem Soc* **2024**, *146* (36), 24935. https://doi.org/10.1021/jacs.4c06202.

(5) Xia, P.; Sun, B.; Biondi, M.; Xu, J.; Atan, O.; Imran, M.; Hassan, Y.; Liu, Y.; Pina, J. M.; Najarian, A. M.; Grater, L.; Bertens, K.; Sagar, L. K.; Anwar, H.; Choi, M. J.; Zhang, Y.; Hasham, M.; García de Arquer, F. P.; Hoogland, S.; Wilson, M. W. B.; Sargent, E. H. Sequential Co-Passivation in InAs Colloidal Quantum Dot Solids Enables Efficient NearInfrared Photodetectors. *Advanced Materials* **2023**, *35* (28), 2301842. https://doi.org/10.1002/adma.202301842.

(6) Shin, D.; Jeong, H.; Kim, J.; Jang, E.; Park, Y.; Jeong, S. High Performance Infrared InAs Colloidal Quantum Dot Photodetector with 79% EQE Enabled by an Extended Absorber Layer. *Adv Opt Mater* **2025**, *13* (1), 2401931. https://doi.org/10.1002/adom.202401931.

(7) Vafaie, M.; Fan, J. Z.; Morteza Najarian, A.; Ouellette, O.; Sagar, L. K.; Bertens, K.; Sun, B.; García de Arquer, F. P.; Sargent, E. H. Colloidal Quantum Dot Photodetectors with 10-Ns Response Time and 80% Quantum Efficiency at 1,550 Nm. *Matter* **2021**, *4* (3), 1042–1053. https://doi.org/10.1016/j.matt.2020.12.017.

(8) Yang, J.; Hu, H.; Lv, Y.; Yuan, M.; Wang, B.; He, Z.; Chen, S.; Wang, Y.; Hu, Z.; Yu, M.; Zhang, X.; He, J.; Zhang, J.; Liu, H.; Hsu, H. Y.; Tang, J.; Song, H.; Lan, X. LigandEngineered HgTe Colloidal Quantum Dot Solids for Infrared Photodetectors. *Nano Lett* **2022**, *22* (8), 3465–3472. https://doi.org/10.1021/acs.nanolett.2c00950.

(9) Parmar, D. H.; Rehl, B.; Atan, O.; Hoogland, S.; Sargent, E. H. Transient Measurements and Simulations Correlate Exchange Ligand Concentration and Trap States in Colloidal Quantum Dot Photodetectors. *ACS Appl Mater Interfaces* **2023**, *15* (51), 59931–59938. https://doi.org/10.1021/acsami.3c14611.

(10) Gong, W.; Wang, P.; Deng, W.; Zhang, X.; An, B.; Li, J.; Sun, Z.; Dai, D.; Liu, Z.; Li, J.; Zhang, Y. Limiting Factors of Detectivity in Near-Infrared Colloidal Quantum Dot Photodetectors. *ACS Appl Mater Interfaces* **2022**, *14* (22), 25812–25823. https://doi.org/10.1021/acsami.2c06620.

(11) Bozyigit, D.; Volk, S.; Yarema, O.; Wood, V. Quantification of Deep Traps in Nanocrystal Solids, Their Electronic Properties, and Their Influence on Device Behavior. *Nano Lett* **2013**, *13* (11), 5284–5288. https://doi.org/10.1021/nl402803h.

(12) Bozyigit, D.; Lin, W. M. M.; Yazdani, N.; Yarema, O.; Wood, V. A Quantitative Model for Charge Carrier Transport, Trapping and Recombination in Nanocrystal-Based Solar Cells. *Nat Commun* **2015**, *6* (6180). https://doi.org/10.1038/ncomms7180.

(13) Almeida, G.; Ubbink, R. F.; Stam, M.; du Fossé, I.; Houtepen, A. J. InP Colloidal Quantum Dots for Visible and Near-Infrared Photonics. *Nat Rev Mater* **2023**, *8* (11), 742–758. https://doi.org/10.1038/s41578-023-00596-4.

(14) Won, Y. H.; Cho, O.; Kim, T.; Chung, D. Y.; Kim, T.; Chung, H.; Jang, H.; Lee, J.; Kim, D.; Jang, E. Highly Efficient and Stable InP/ZnSe/ZnS Quantum Dot Light-Emitting Diodes. *Nature* **2019**, *575* (7784), 634–638. https://doi.org/10.1038/s41586-019-1771-5.

(15) Zhang, X.; Ogitsu, T.; Wood, B. C.; Pham, T. A.; Ptasinska, S. Oxidation-Induced Polymerization of InP Surface and Implications for Optoelectronic Applications. *Journal of Physical Chemistry C* **2019**, *123* (51), 30893–30902. https://doi.org/10.1021/acs.jpcc.9b07260.

(16) Baquero, E. A.; Virieux, H.; Swain, R. A.; Gillet, A.; Cros-Gagneux, A.; Coppel, Y.;

Chaudret, B.; Nayral, C.; Delpech, F. Synthesis of Oxide-Free InP Quantum Dots: Surface Control and H2-Assisted Growth. *Chemistry of Materials* **2017**, *29* (22), 9623–9627. https://doi.org/10.1021/acs.chemmater.7b04069.

(17) Kirkwood, N.; Monchen, J. O. V.; Crisp, R. W.; Grimaldi, G.; Bergstein, H. A. C.; Du Fossé, I.; Van Der Stam, W.; Infante, I.; Houtepen, A. J. Finding and Fixing Traps in II-VI and III-V Colloidal Quantum Dots: The Importance of Z-Type Ligand Passivation. *J Am Chem Soc* **2018**, *140* (46), 15712–15723. https://doi.org/10.1021/jacs.8b07783.

(18) Cho, E.; Kim, T.; Choi, S. myeong; Jang, H.; Min, K.; Jang, E. Optical Characteristics of the Surface Defects in InP Colloidal Quantum Dots for Highly Efficient Light-Emitting Applications. *ACS Appl Nano Mater* **2018**, *1* (12), 7106–7114. https://doi.org/10.1021/acsanm.8b01947.

(19) Dai, P.; Wang, Z.; Tang, Z.; Zhang, Z.; Wang, Y.; Yang, X.; Jiang, J.; Zhang, Y.; Yang, H. Bismuth-Doped Ag2Te Colloidal Quantum Dots for High-Performance Shortwave-Infrared Photodetectors. *Inorg Chem* **2025**, *64* (28), 14637–14643. https://doi.org/10.1021/acs.inorgchem.5c02229.

(20) Asor, L.; Liu, J.; Xiang, S.; Tessler, N.; Frenkel, A. I.; Banin, U. Zn-Doped P-Type InAs Nanocrystal Quantum Dots. *Advanced Materials* **2023**, *35* (5), 2208332. https://doi.org/10.1002/adma.202208332.

(21) Mundy, M. E.; Eagle, F. W.; Hughes, K. E.; Gamelin, D. R.; Cossairt, B. M. Synthesis and Spectroscopy of Emissive, Surface-Modified, Copper-Doped Indium Phosphide Nanocrystals. *ACS Mater Lett* **2020**, *2* (6), 576–581. https://doi.org/10.1021/acsmaterialslett.0c00112.

(22) Park, Y. S.; Lim, J.; Klimov, V. I. Asymmetrically Strained Quantum Dots with NonFluctuating Single-Dot Emission Spectra and Subthermal Room-Temperature Linewidths. *Nat Mater* **2019**, *18* (3), 249–255. https://doi.org/10.1038/s41563-018-0254-7.

(23) Song, Y.; Liu, R.; Wang, Z.; Xu, H.; Ma, Y.; Fan, F.; Voznyy, O.; Du, J. Enhanced Emission Directivity from Asymmetrically Strained Colloidal Quantum Dots. *Sci. Adv* **2022**, *8* (eabl8219), 8219.

(24) Jang, Y.; Shapiro, A.; Isarov, M.; Rubin-Brusilovski, A.; Safran, A.; Budniak, A. K.; Horani, F.; Dehnel, J.; Sashchiuk, A.; Lifshitz, E. Interface Control of Electronic and Optical Properties in IV-VI and II-VI Core/Shell Colloidal Quantum Dots: A Review. *Chemical Communications* **2017**, *53* (6), 1002–1024. https://doi.org/10.1039/c6cc08742f.

(25) Park, N.; Eagle, F. W.; Delarme, A. J.; Monahan, M.; Locurto, T.; Beck, R.; Li, X.; Cossairt, B. M. Tuning the Interfacial Stoichiometry of InP Core and InP/ZnSe Core/Shell Quantum Dots. *Journal of Chemical Physics* **2021**, *155* (8), 084701. https://doi.org/10.1063/5.0060462.

(26) Fang, Y.; Armin, A.; Meredith, P.; Huang, J. Accurate Characterization of Next-Generation Thin-Film Photodetectors. *Nat Photonics* **2019**, *13* (1), 1–4. https://doi.org/10.1038/s41566018-0288-z.

(27) Guo, R.; Zhang, M.; Ding, J.; Liu, A.; Huang, F.; Sheng, M. Advances in Colloidal Quantum Dot-Based Photodetectors. *J Mater Chem C Mater* **2022**, *10* (19), 7404–7422. https://doi.org/10.1039/d2tc00219a.

(28) Kaiser, C.; Zeiske, S.; Meredith, P.; Armin, A. Determining Ultralow Absorption Coefficients of Organic Semiconductors from the Sub-Bandgap Photovoltaic External Quantum Efficiency. *Adv Opt Mater* **2020**, *8* (1), 1901542. https://doi.org/10.1002/adom.201901542.

(29) Armin, A.; Zarrabi, N.; Sandberg, O. J.; Kaiser, C.; Zeiske, S.; Li, W.; Meredith, P. Limitations of Charge Transfer State Parameterization Using Photovoltaic External Quantum Efficiency. *Adv Energy Mater* **2020**, *10* (41), 2001828. https://doi.org/10.1002/aenm.202001828.

(30) Zeiske, S.; Sandberg, O. J.; Zarrabi, N.; Wolff, C. M.; Raoufi, M.; Peña-Camargo, F.; Gutierrez-Partida, E.; Meredith, P.; Stolterfoht, M.; Armin, A. Static Disorder in Lead Halide Perovskites. *Journal of Physical Chemistry Letters* **2022**, *13* (31), 7280–7285. https://doi.org/10.1021/acs.jpclett.2c01652.

(31) Jean, J.; Mahony, T. S.; Bozyigit, D.; Sponseller, M.; Holovský, J.; Bawendi, M. G.; Bulović, V. Radiative Efficiency Limit with Band Tailing Exceeds 30% for Quantum Dot Solar Cells. *ACS Energy Lett* **2017**, *2* (11), 2616–2624. https://doi.org/10.1021/acsenergylett.7b00923.

(32) Erslev, P. T.; Chen, H. Y.; Gao, J.; Beard, M. C.; Frank, A. J.; Van De Lagemaat, J.; Johnson, J. C.; Luther, J. M. Sharp Exponential Band Tails in Highly Disordered Lead Sulfide Quantum Dot Arrays. *Phys Rev B Condens Matter Mater Phys* **2012**, *86* (15), 155313. https://doi.org/10.1103/PhysRevB.86.155313.

(33) Bozyigit, D.; Jakob, M.; Yarema, O.; Wood, V. Deep Level Transient Spectroscopy (DLTS) on Colloidal-Synthesized Nanocrystal Solids. *ACS Appl Mater Interfaces* **2013**, *5* (8), 2915–2919. https://doi.org/10.1021/am400326t.

(34) Jin, Z.; Wang, A.; Zhou, Q.; Wang, Y.; Wang, J. Detecting Trap States in Planar PbS Colloidal Quantum Dot Solar Cells. *Sci Rep* **2016**, *6*. https://doi.org/10.1038/srep37106.

(35) Chuang, C. H. M.; Maurano, A.; Brandt, R. E.; Hwang, G. W.; Jean, J.; Buonassisi, T.; Bulović, V.; Bawendi, M. G. Open-Circuit Voltage Deficit, Radiative Sub-Bandgap States, and Prospects in Quantum Dot Solar Cells. *Nano Lett* **2015**, *15* (5), 3286–3294. https://doi.org/10.1021/acs.nanolett.5b00513.

(36) Kahmann, S.; Sytnyk, M.; Schrenker, N.; Matt, G. J.; Spiecker, E.; Heiss, W.; Brabec, C. J.; Loi, M. A. Revealing Trap States in Lead Sulphide Colloidal Quantum Dots by Photoinduced Absorption Spectroscopy. *Adv Electron Mater* **2018**, *4* (1), 1700348. https://doi.org/10.1002/aelm.201700348.

(37) Llusar, J.; du Fossé, I.; Hens, Z.; Houtepen, A.; Infante, I. Surface Reconstructions in II-VI Quantum Dots. *ACS Nano* **2024**, *18* (2), 1563–1572. https://doi.org/10.1021/acsnano.3c09265.

(38) Shockley, W.; Queisser, H. J. Detailed Balance Limit of Efficiency of P-n Junction Solar Cells. *J Appl Phys* **1961**, *32* (3), 510–519. https://doi.org/10.1063/1.1736034.

(39) Rau, U. Reciprocity Relation between Photovoltaic Quantum Efficiency and Electroluminescent Emission of Solar Cells. *Phys Rev B Condens Matter Mater Phys* **2007**, *76* (8), 085303. https://doi.org/10.1103/PhysRevB.76.085303.

(40) Zarrabi, N.; Sandberg, O. J.; Zeiske, S.; Li, W.; Riley, D. B.; Meredith, P.; Armin, A. ChargeGenerating Mid-Gap Trap States Define the Thermodynamic Limit of Organic Photovoltaic Devices. *Nat Commun* **2020**, *11* (5567), 5567. https://doi.org/10.1038/s41467-020-19434-0.

For Table of Contents Only